Taylor & Francis
Taylor & Francis Group

Vehicle System Dynamics
International Journal of Vehicle Mechanics and Mobility

ISSN: 0042-3114 (Print) 1744-5159 (Online) Journal homepage: http://www.tandfonline.com/loi/nvsd20

Simultaneous dynamic system estimation and optimal control of vehicle active suspension

Tamer Attia, Kyriakos G. Vamvoudakis, Kevin Kochersberger, John Bird & Tomonari Furukawa

To cite this article: Tamer Attia, Kyriakos G. Vamvoudakis, Kevin Kochersberger, John Bird & Tomonari Furukawa (2018): Simultaneous dynamic system estimation and optimal control of vehicle active suspension, Vehicle System Dynamics, DOI: 10.1080/00423114.2018.1521000

To link to this article: https://doi.org/10.1080/00423114.2018.1521000

Published online: 19 Sep 2018.

VEHICLE SYSTEM DYNAMICS
https://doi.org/10.1080/00423114.2018.1521000

Simultaneous dynamic system estimation and optimal control of vehicle active suspension

Tamer Attia [a], Kyriakos G. Vamvoudakis [b], Kevin Kochersberger[a], John Bird[a] and Tomonari Furukawa [a]

[a]Department of Mechanical Engineering, Virginia Polytechnic Institute and State University, Blacksburg, VA, USA; [b]School of Aerospace Engineering, Georgia Institute of Technology, Atlanta, GA, USA

ABSTRACT

This paper proposes a combined observer/controller method that estimates the states and simultaneously improves the ride comfort and stability of a full vehicle active suspension system using a single inertial measurement unit (IMU) in the presence of noise and centre of gravity uncertainties. The derived model is based on a channel-by-channel estimation technique using filtered white noise excitation signals on all the wheels, as well as active suspension actuators. The transfer functions of the vehicle system are estimated by analysing the IMU signals in the frequency domain. The derived result is then used in a linear quadratic regulator to calculate the actuators' forces to improve the vehicle's ride comfort and road holding stability within the limits of the rattle space. The simulation results show the efficacy of the proposed approach. Specifically, the observer estimates the actual behaviour of the vehicle with 95% accuracy with up to 20% uncertainty. Finally, a parametric study has been investigated to ascertain the applicability of the proposed approach in estimating the vehicle dynamics with simultaneously improving the ride comfort and road holding stability.

ARTICLE HISTORY
Received 26 September 2017
Revised 10 June 2018
Accepted 31 August 2018

KEYWORDS
Optimal control; active suspension; observer design; uncertainties

1. Introduction

In recent years, particular attention has been paid to improve vehicle stability and ride comfort by using active suspension systems [1–7]. Such systems improve ride comfort by isolating the sprung mass from external disturbances that can be caused by terrain and other irregularities. They achieve vehicle stability, namely, handling stability [8], by ensuring a firm contact between tires and the road at all times. The challenge is however that the suspension spring needs to be stiff to guarantee and satisfy several road holding criteria and in the same time the spring needs to be soft to mitigate disturbances induced by terrain and weather. In a classical vehicle suspension setting [9], the spring and the damping parameters cannot be efficiently controlled and adapted to different driving conditions. However, by using an active suspension system with actuators that work along with the spring and damper, one can accumulate or dissipate energy from the system [5,10,11].

CONTACT Tamer Attia tamer11@vt.edu

Active suspension systems with control techniques [12–14] have been introduced to improve the performance, handling characteristics and riding of the vehicle by controlling the suspension system. It has been shown that actuators controlled by optimisation-based control techniques [15] are efficient for controlling the active suspension system while guaranteeing optimal performance. But in such optimisation-based control techniques one needs to have full-state information to successfully control the actual model while such information is not always available in practice due to sensor cost, complexity, uncertainties, noise, or even measurement restrictions. Several observer-based techniques [13,16–18] and modified Kalman filters [16,19–24] have been used to overcome such problems. A survey on how to control active and semi-active suspension system is given in [12]. In this survey, the authors used a quarter-car model for reviewing the controller design potential benefits and limitations through the application of optimal control theory with an LQ-based cost function. The work of Yamada et al. [13] has introduced a robust control technique for an active suspension while also considering actuator constraints and uncomfortable frequency bands for bounce and pitch accelerations of the sprung mass. In [7], a nonlinear controller was used for controlling the active suspension of a quarter-car model with the ultimate goal to improve ride comfort while trying to keep the suspension deflection within the limits of the rattle space.

In [16], the authors used a Kalman filter to estimate the system states, the estimator was based on somewhat idealised assumption of knowing exactly the road profile. The work of Wenzel et al. [19] proposed a dual extended Kalman filter to estimate the vehicle states and other parameters. In order to achieve that, the authors incorporated two parallel filters, one for estimating the main vehicle parameters and the other for estimating the vehicle states. This technique has been shown to improve the accuracy of the estimated parameters and can handle the model uncertainties. The works of Pletschen et al. [21–23] proposed similar approaches with an accuracy of the estimated states being between 70% and 90%.

The recent work of García and Patino [25] has used a Kalman filter, a particle filter and artificial neural networks to estimate different states of the quarter-car model by incorporating an IMU. However, the effect of measurement uncertainties and the accuracy of the state estimation can negatively affect the higher order models. A continuous-time system identification technique in a half-car model has been proposed in [26] to estimate the vehicle suspension model. The aforementioned papers did not obtain the dynamic parameters of the actual vehicle model while taking into account the presence of measurement uncertainties. Our work is motivated by such limitations.

This paper presents a method for estimating the vehicle dynamic model by using system identification techniques with a single point sensor and centre of gravity (CG) uncertainty. A combined observer/controller method has been developed to estimate the states and simultaneously improve the ride comfort and handling stability of a full vehicle active suspension system. We introduce an efficient solution to estimate and control the actual full vehicle with a limited number of sensors in the presence of noise and CG position uncertainties. A single IMU has been placed on the sprung mass, which leads us to the successful estimation of all the states while at the same time controlling efficiently the suspension system to improve ride comfort and handling stability. To achieve this, we use two steps, first, estimating the vehicle dynamic model by analysing all input–output paths of the transfer functions in the frequency domain, and second, applying a Kalman filter and a linear quadratic regulator (LQR) on the estimated state-space model. The latter, allows us

to calculate the optimal forces to improve the vehicle performance index, i.e. ride comfort and road holding stability.

The remainder of the paper is structured as follows. In Section 2, we formulate the problem and introduce the full vehicle dynamic model with the active suspension system. The proposed vehicle model takes into account uncertainties in the position of the centre of gravity. Assuming now that the vehicle dynamics are unknown, Section 3 provides a method of estimating the mathematical model of the vehicle, which is based on system identification techniques. In Section 4, we design an observer based on a Kalman filter for estimating the vehicle states and feed the result in the optimal control algorithm in order to control the active suspension system. Section 5, provides a numerical simulation for estimating the vehicle dynamics behaviour while controlling optimally the suspension system to simultaneously improve the ride comfort and road holding stability within the limits of the rattle space. Finally, Section 6 concludes and discusses future work.

Notation: The notation used here is standard. $\lambda(A)$ is the eigenvalues of a matrix A, $(.)^{\mathrm{T}}$ denotes the transpose of a matrix, $\bar{z}$ is the conjugate of the complex number z, $\hat{A}$ is the estimated value of A in continuous time, $\hat{A}_d$ is the estimated value of A in discrete time. The superscript $*$ is used to denote the optimal solution of an optimisation, the superscript/subscript k is used to denote a value at discrete time k, the subscript s denotes the sprung mass value while the subscript m denotes the IMU signals. $A \succeq 0$ denotes that the matrix A is positive semidefinite and the notation $A \succ 0$ to denote that the matrix A is positive definite. Finally, $H(s)$ denotes the transfer function H in s-domain and $H(z)$ denotes the transfer function in z-domain.

2. Problem formulation

A linear full vehicle model with seven degree of freedom (DOF) as shown in Figure 1 is considered for this research because it is sufficient and enough for capturing the vehicle dynamical behaviour [27–29]. The authors in [29] compared the results of a linear vehicle model with a measured data through an experimental test using the same road input. These results show a close match between the simulation model and the experimental test, which gives credence to use a linear vehicle model for estimating the states and optimally controlling the active suspension system to enhance ride comfort and vehicle stability.

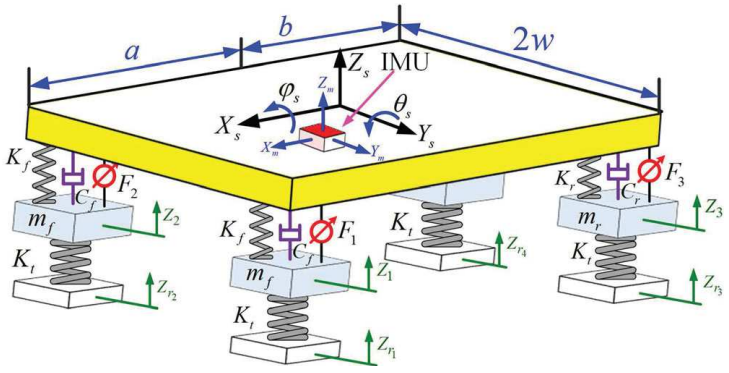

Figure 1. The full vehicle model with the active suspension system.

The full vehicle model consists of a sprung mass with three DOF in the vertical Z_s-axis (bounce), rotation about X_s-axis (roll) and rotation about Y_s-axis (pitch), with four unsprung masses in front left, front right, rear left and rear right which have one DOF in the vertical directions z_1, z_2, z_3, z_4 at front left, front right, rear left and rear right, respectively.

The dynamic equations of the full vehicle system can be derived using the Newton's second law as follows [4,30–32],

$$\begin{aligned} m_s\ddot{z_s} &= F_{fl} + F_{fr} + F_{rl} + F_{rr}, \\ I_y\ddot{\theta_s} &= -aF_{fl} - aF_{fr} + bF_{rl} + bF_{rr}, \\ I_x\ddot{\phi_s} &= wF_{fl} - wF_{fr} + wF_{rl} - wF_{rr}, \\ m_f\ddot{z_1} &= -F_{fl} - k_t(z_1 - z_{r_1}), \\ m_f\ddot{z_2} &= -F_{fr} - k_t(z_2 - z_{r_2}), \\ m_r\ddot{z_3} &= -F_{rl} - k_t(z_3 - z_{r_3}), \\ m_r\ddot{z_4} &= -F_{rr} - k_t(z_4 - z_{r_4}), \end{aligned} \tag{1}$$

where m_s is the mass of the vehicle body, I_x is the roll moment, I_y is the pitch moment of inertia about the centre of mass, ϕ_s, θ_s are the roll and pitch angles of the sprung mass, a,b are the CG locations of the front and rear axles, $2w$ is the wheel track, m_f, m_r stand for the unsprung mass on front and rear, respectively, k_t is the tire spring stiffness, $z_{r_1}, z_{r_2}, z_{r_3}, z_{r_4}$ are the road displacements at front left, front right, rear left and rear right respectively, and $F_{fl}, F_{fr}, F_{rl}, F_{rr}$ are the forces generated between the sprung mass at each corner and the unsprung masses at front left, front right, rear left and rear right, respectively.

The forces are defined as follows,

$$\begin{aligned} F_{fl} &:= -k_f(z_{fl} - z_1) - c_f(\dot{z}_{fl} - \dot{z}_1) + F_1, \\ F_{fr} &:= -k_f(z_{fr} - z_2) - c_f(\dot{z}_{fr} - \dot{z}_2) + F_2, \\ F_{rl} &:= -k_r(z_{rl} - z_3) - c_r(\dot{z}_{rl} - \dot{z}_3) + F_3, \\ F_{rr} &:= -k_r(z_{rr} - z_4) - c_r(\dot{z}_{rr} - \dot{z}_4) + F_4, \end{aligned} \tag{2}$$

where k_f is the front spring stiffness and k_r is the rear spring stiffness, c_f, c_r are the front and the rear shock absorber damping coefficients, and F_1, F_2, F_3, F_4 are the active suspension actuators at the front left, the front right, the rear left and the rear right, respectively.

The dynamics can be simplified by applying the following assumption.

Assumption 1: The angles θ_s and ϕ_s, are small enough and we can write $\sin\theta_s \approx \theta_s$, $\sin\phi_s \approx \phi_s$.

Based on Assumption 1 the dynamic vertical displacements of the sprung mass corners can be written as,

$$\begin{aligned} z_{fl} &:= z_s + w\phi_s - a\theta_s, \\ z_{fr} &:= z_s - w\phi_s - a\theta_s, \\ z_{rl} &:= z_s + w\phi_s + b\theta_s, \\ z_{rr} &:= z_s - w\phi_s + b\theta_s. \end{aligned} \tag{3}$$

For simplicity let us use the following state-space assignments,

$$\begin{aligned}
&x_1 := z_{fl} - z_1, \quad x_2 := z_{fr} - z_2, \quad x_3 := z_{rl} - z_3, \quad x_4 := z_{rr} - z_4,\\
&x_5 := z_1 - z_{r_1}, \quad x_6 := z_2 - z_{r_2}, \quad x_7 := z_3 - z_{r_3}, \quad x_8 := z_4 - z_{r_4},\\
&x_9 := \dot{z}_s, \quad x_{10} := \dot{\theta}_s, \quad x_{11} := \dot{\phi}_s,\\
&x_{12} := \dot{z}_1, \quad x_{13} := \dot{z}_2, \quad x_{14} := \dot{z}_3, \quad x_{15} := \dot{z}_4.
\end{aligned}$$

The state-space assignments rewrite (1)–(3) as follows (see Appendix for more details),

$$\begin{aligned}
\dot{X} &= AX + B_e Q + B_f F,\\
Y &= CX + D_e Q + D_f F,
\end{aligned} \tag{4}$$

where,

$$\begin{aligned}
X &= \begin{bmatrix} x_1 & x_2 & x_3 & \dots & x_{12} & x_{13} & x_{14} \end{bmatrix}^{\mathrm{T}},\\
Y &= \begin{bmatrix} \ddot{z}_s & \ddot{\theta}_s & \ddot{\phi}_s \end{bmatrix}^{\mathrm{T}},\\
Q &= \begin{bmatrix} \dot{z}_{r_1} & \dot{z}_{r_2} & \dot{z}_{r_3} & \dot{z}_{r_4} \end{bmatrix}^{\mathrm{T}}, \quad F = \begin{bmatrix} F_1 & F_2 & F_3 & F_4 \end{bmatrix}^{\mathrm{T}}.
\end{aligned}$$

The active suspension system is designed to improve ride comfort and road holding stability within the limits of the suspension deflection. Hence, three aspects are going to be considered in our work:

(1) Ride comfort which is related to the sprung mass bounce, roll and pitch accelerations. By reducing these accelerations, good ride comfort will be experienced by the passengers.
(2) Road holding stability which is defined by the tire dynamic load; where to ensure vehicle stability, the dynamic tire load should not exceed its static load to maintain uninterrupted contact with the road, which can be expressed as the relative tire loads and is given by,

$$\begin{aligned}
\eta_1 &:= \frac{k_t(z_1 - z_{r_1})}{g\left(((bm_s)/(2(a+b))) + m_f\right)} < 1,\\
\eta_2 &:= \frac{k_t(z_2 - z_{r_2})}{g\left(((bm_s)/(2(a+b))) + m_f\right)} < 1,\\
\eta_3 &:= \frac{k_t(z_3 - z_{r_3})}{g\left(((am_s)/(2(a+b))) + m_r\right)} < 1,\\
\eta_4 &:= \frac{k_t(z_4 - z_{r_4})}{g\left(((am_s)/(2(a+b))) + m_r\right)} < 1,
\end{aligned}$$

where $\eta_1, \eta_2, \eta_3, \eta_4$ are the relative tire loads at front left, front right, rear left and rear right, and g is the gravitational acceleration.

(3) And finally, the suspension deflection which is limited by the available rattle space as follow,

$$\mu_1 := \frac{|z_{fl} - z_1|}{z_{\max}} < 1, \quad \mu_2 := \frac{|z_{fr} - z_2|}{z_{\max}} < 1,$$
$$\mu_3 := \frac{|z_{rl} - z_3|}{z_{\max}} < 1, \quad \mu_4 := \frac{|z_{rr} - z_4|}{z_{\max}} < 1,$$

where $\mu_1, \mu_2, \mu_3, \mu_4$ are the relative suspension deflections at front left, front right, rear left and rear right, and z_{max} is the maximum rattle space hard limit.

Figure 2, in addition to Figure 1, shows the location of the IMU. The measured signals for bounce acceleration, roll and pitch velocities are governed by the measurement model of IMU, where the position uncertainties are denoted by r_m. We differentiate the IMU angular velocities to get the angular accelerations.

Referring to (5)–(7), the IMU position, the velocity and the acceleration vectors r, $\dot{r}$, and $\ddot{r}$ respectively, can be calculated with respect to the world-fixed frame (X_G, Y_G, Z_G) as,

$$r = r_s + A_r(\phi, \theta)\, r_m, \tag{5}$$

$$\dot{r} = \dot{r}_s + \left(\dot{\phi}_s \begin{bmatrix} 0 & 0 & 0 \\ \cos\phi_s \sin\theta_s & -\sin\phi_s & -\cos\phi_s \cos\theta_s \\ \sin\phi_s \sin\theta_s & \cos\phi_s & -\sin\phi_s \cos\theta_s \end{bmatrix} + \dot{\theta}_s \begin{bmatrix} -\sin\theta_s & 0 & \cos\theta_s \\ \sin\phi_s \cos\theta_s & 0 & \sin\phi_s \sin\theta_s \\ -\cos\phi_s \cos\theta_s & 0 & -\cos\phi_s \sin\theta_s \end{bmatrix} \right) r_m, \tag{6}$$

and,

$$\ddot{r} = \ddot{r}_s + \left(\ddot{\phi}_s \begin{bmatrix} 0 & 0 & 0 \\ \cos\phi_s \sin\theta_s & -\sin\phi_s & -\cos\phi_s \cos\theta_s \\ \sin\phi_s \sin\theta_s & \cos\phi_s & -\sin\phi_s \cos\theta_s \end{bmatrix} - \dot{\phi}_s^2 \begin{bmatrix} 0 & 0 & 0 \\ \sin\phi_s \sin\theta_s & \cos\phi_s & -\sin\phi_s \cos\theta_s \\ -\cos\phi_s \sin\theta_s & \sin\phi_s & \cos\phi_s \cos\theta_s \end{bmatrix} \right)$$

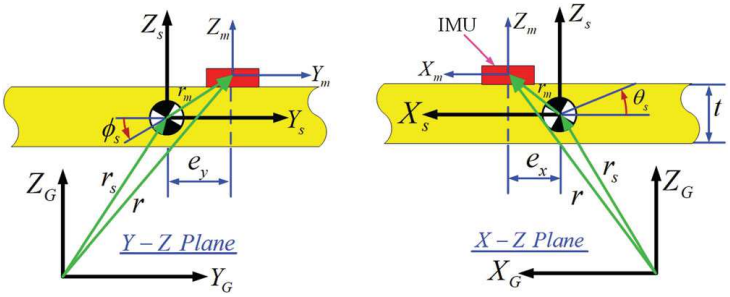

Figure 2. An IMU is placed on the sprung mass with distance $(e_x, e_y, t/2)$ from the sprung mass centre of gravity. The IMU signals are different from the actual signals.

$$+\ddot{\theta}_s\begin{bmatrix}-\sin\theta_s & 0 & \cos\theta_s\\ \sin\phi_s\cos\theta_s & 0 & \sin\phi_s\sin\theta_s\\ -\cos\phi_s\cos\theta_s & 0 & -\cos\phi_s\sin\theta_s\end{bmatrix} \tag{7}$$

$$-\dot{\theta}_s^2\begin{bmatrix}\cos\theta_s & 0 & \sin\theta_s\\ \sin\phi_s\sin\theta_s & 0 & -\sin\phi_s\cos\theta_s\\ -\cos\phi_s\sin\theta_s & 0 & \cos\phi_s\cos\theta_s\end{bmatrix}$$

$$+2\dot{\phi}_s\dot{\theta}_s\begin{bmatrix}0 & 0 & 0\\ \cos\phi_s\cos\theta_s & 0 & \cos\phi_s\sin\theta_s\\ \sin\phi_s\cos\theta_s & 0 & \sin\phi_s\sin\theta_s\end{bmatrix}\Bigg)r_m,$$

where the rotation matrix is,

$$A_{\mathrm{r}}(\phi,\theta)=\begin{bmatrix}\cos\theta_s & 0 & \sin\theta_s\\ \sin\phi_s\sin\theta_s & \cos\phi_s & -\sin\theta_s\cos\theta_s\\ -\cos\phi_s\sin\theta_s & \sin\phi_s & \cos\theta_s\cos\theta_s\end{bmatrix},$$

and the position vectors are defined as,

$$r:=\begin{bmatrix}X_{\mathrm{m}} & Y_{\mathrm{m}} & Z_{\mathrm{m}}\end{bmatrix}^{\mathrm{T}},\quad r_s:=\begin{bmatrix}X_{\mathrm{s}} & Y_{\mathrm{s}} & Z_{\mathrm{s}}\end{bmatrix}^{\mathrm{T}},\quad r_m:=\begin{bmatrix}e_{\mathrm{x}} & e_{\mathrm{y}} & 0.5t\end{bmatrix}^{\mathrm{T}}.$$

In order to model a potentially noisy IMU, a white Gaussian noise with zero mean and variance σ_ν is added to the IMU signals as,

$$y_{\mathrm{m}}=s_{\mathrm{m}}+\nu, \tag{8}$$

where,

$$s_{\mathrm{m}}:=\begin{bmatrix}\ddot{z}_{\mathrm{m}} & \ddot{\theta}_{\mathrm{s}} & \ddot{\phi}_{\mathrm{s}}\end{bmatrix}^{\mathrm{T}},\quad \nu\sim\mathcal{N}(0,\sigma_\nu^2).$$

By writing (8) in the frequency domain one has,

$$Y_{\mathrm{m}}(s)=H(s)U(s)+\nu,\quad U(s)=\begin{bmatrix}Q & F\end{bmatrix}^{\mathrm{T}}, \tag{9}$$

where $H(s)$ is the transfer function and $U(s)$ is the input signal.

Since the IMU signals are in discrete-time domain, the bilinear transformation is employed to transform the system from continuous-time to discrete-time [33]. In other words, all transfer functions in (9) can be written as,

$$H(z)=H(s)\left(\frac{2}{T_s}\left(\frac{z-1}{z+1}\right)\right), \tag{10}$$

where $H(z)$ is the transfer function in the discrete-time domain, and $T_s\in\mathbb{R}^+$ is the sampling time.

3. Vehicle dynamic model estimation

The system identification technique proposed in this paper is based on exciting the full vehicle model at the wheels, and the active suspension actuators. A diagram of the proposed technique is shown in Figure 3.

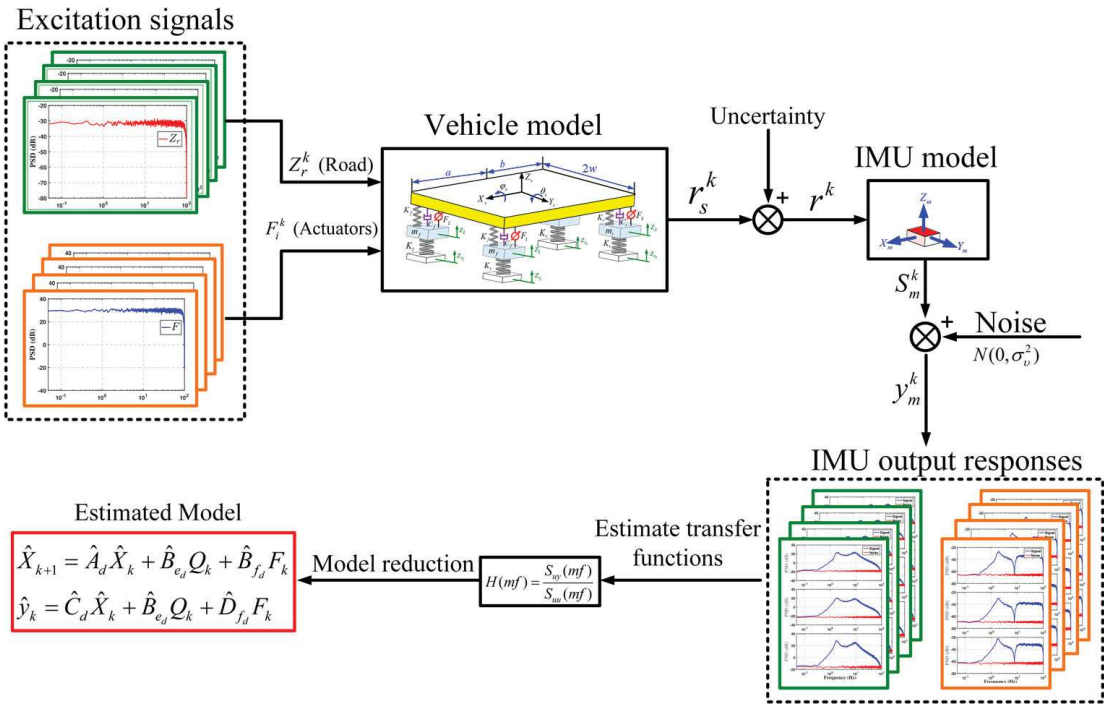

Figure 3. Dynamic model estimation diagram. It is shown the steps of estimating the vehicle dynamic model using only IMU.

The excitation signals are filtered white noises with zero mean and variance σ_u [34] as follows,

$$u(t) = L(q)e(t),$$

where, q is the backward shift operator, i.e. $q = z^{-1}$, and $L(q)$ is a first order low pass filter, i.e. $L(z^{-1}) = (z^{-1} + 1)/((\pi - 2/\pi)z^{-1} - (2/\pi))$, with breaking frequency $\omega_b = \pi/T_s$ used to eliminate the false response at the Nyquist frequency.

The channel-by-channel excitation signals are shown in Figure 4, where, filtered signals of amplitude $|Z_r| \leq 0.1$ m and frequency 0.05:100 Hz, and of amplitude $|F_i| \leq 100$ N and frequency 0.05:100 Hz are generated at the wheels and the actuators, respectively.

During this process, the excitations and the IMU signals will be recorded for further analysis. Here, the transfer functions are estimated by analysing the IMU signals in the frequency domain to determine the locations and numbers of poles and zeros. In order to estimate the noise power of the IMU, all the excitation signals are set to zero, i.e. $Z_r = 0$ and $F_i = 0$, and the IMU signals are recorded at the steady-state in order to calculate the bias and the standard deviation σ_v as a calibration process for the IMU.

The noise power can now be estimated by using,

$$\sigma_v^2 = E\Big[y_m^2 | s_m = 0\Big].$$

The IMU response signal and the noise in the time and the frequency domains are shown in Figure 5 during the excitation process, where, the discrete Fourier transform [35] is used to transform the signals from the time to the frequency domain and to calculate the power spectral density of the IMU signals.

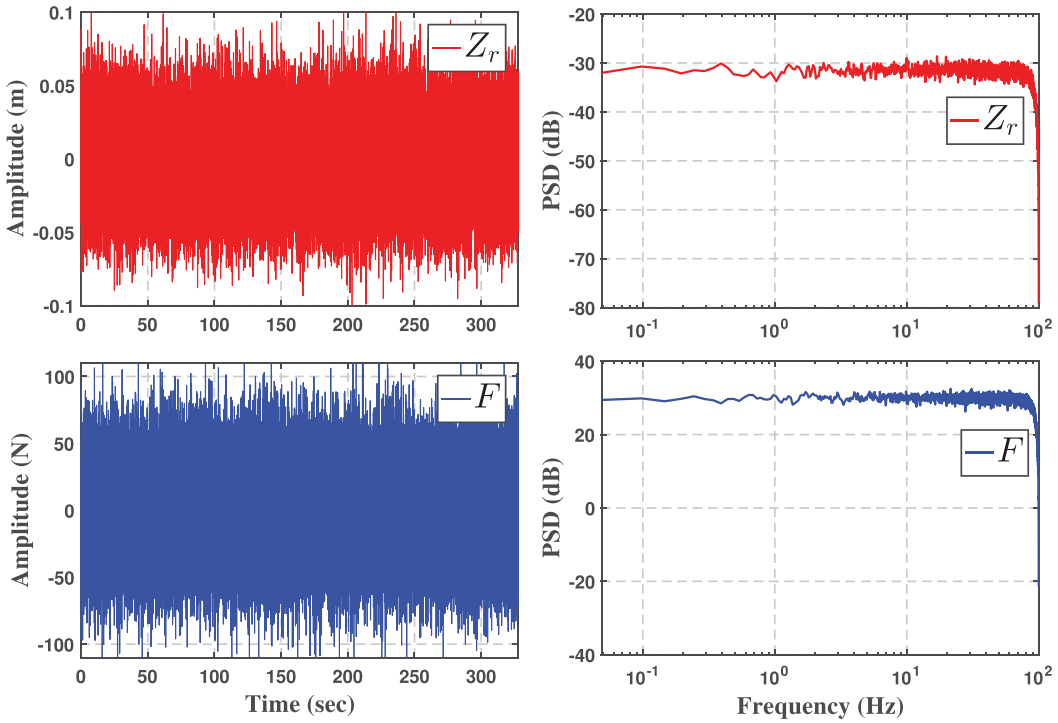

Figure 4. The excitation signals in time and frequency domains.

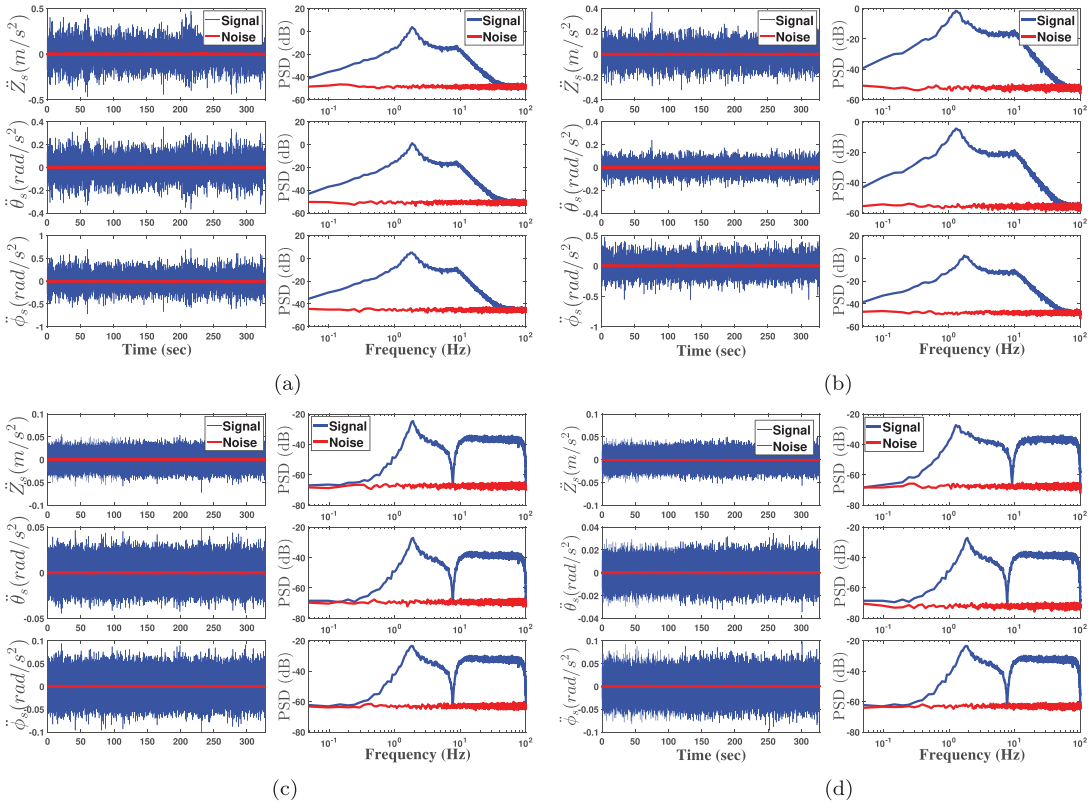

Figure 5. IMU output responses during the excitation process. (a) Front left wheel, (b) Rear right wheel, (c) Front left actuator, (d) Rear right actuator.

Assuming that the noise ν is uncorrelated with the output signal s_m, then the power of the output signals can be calculated from (8) as follows,

$$\sigma_y^2 = E\left[y_m^2\right] = E\left[(S_m + \nu)^2\right] = E\left[S_m^2 + 2S_m\nu + \nu^2\right],$$
$$\sigma_y^2 = E\left[s_m^2\right] + E\left[\nu^2\right] = \sigma_s^2 + \sigma_\nu^2,$$
$$\sigma_s^2 = \sigma_y^2 - \sigma_\nu^2.$$

In order to identify the unknown system dynamics given by (4), we have to estimate 24 input–output paths of frequency response functions (FRFs) in (11),

$$\begin{bmatrix} Z_{\mathrm{m}}^a \\ \theta_{\mathrm{s}}^a \\ \phi_{\mathrm{s}}^a \end{bmatrix} = \begin{bmatrix} H_{11} & H_{12} & \cdots & H_{17} & H_{18} \\ H_{21} & H_{22} & \cdots & H_{27} & H_{28} \\ H_{31} & H_{32} & \cdots & H_{37} & H_{38} \end{bmatrix} \begin{bmatrix} Z_{\mathrm{r}_1} \\ \vdots \\ Z_{\mathrm{r}_4} \\ F_1 \\ \vdots \\ F_4 \end{bmatrix}, \tag{11}$$

where $Z_{\mathrm{m}}^a, \theta_{\mathrm{s}}^a, \phi_{\mathrm{s}}^a$ represent the acceleration values of the IMU in frequency domain.

After applying the discrete Fourier transform, we can rewrite (9) as,

$$Y_{\mathrm{m}}(mf) = H(mf)U(mf) + \nu(mf), \tag{12}$$

where f is the frequency resolution given as $f = 1/NT_s$, and N, is the number of data samples used.

The next step is to multiply (12) with the input conjugate $\bar{U}$ while assuming that the input is uncorrelated with the noise signal to write,

$$\bar{U}(mf)Y_{\mathrm{m}}(mf) = H(mf)\bar{U}(mf)U(mf) + \bar{U}(mf)\nu(mf),$$
$$S_{\mathrm{uy}}(mf) = H(mf)S_{\mathrm{uu}}(mf) + S_{\mathrm{u}\nu}(mf). \tag{13}$$

Using (13), the FRF can be estimated as follows,

$$H(mf) = \frac{S_{\mathrm{uy}}(mf)}{S_{\mathrm{uu}}(mf)}, \tag{14}$$

where $S_{\mathrm{uu}}(mf), S_{\mathrm{uy}}(mf)$ are the auto-spectrum and cross-spectrum of the input–input and input–output signals respectively.

From (11) and (14), the FRFs can be estimated as,

$$H_{11}(mf) = \frac{S_{\dot{Z}_{r_1}\ddot{Z}_m}(mf)}{S_{\dot{Z}_{r_1}\dot{Z}_{r_1}}(mf)}, \quad H_{12}(mf) = \frac{S_{\dot{Z}_{r_2}\ddot{Z}_m}(mf)}{S_{\dot{Z}_{r_2}\dot{Z}_{r_2}}(mf)}, \quad H_{13}(mf) = \frac{S_{\dot{Z}_{r_3}\ddot{Z}_m}(mf)}{S_{\dot{Z}_{r_3}\dot{Z}_{r_3}}(mf)},$$
$$H_{14}(mf) = \frac{S_{\dot{Z}_{r_4}\ddot{Z}_m}(mf)}{S_{\dot{Z}_{r_4}\dot{Z}_{r_4}}(mf)}, \quad H_{15}(mf) = \frac{S_{F_1\ddot{Z}_m}}{S_{F_1F_1}(mf)}, \quad H_{16}(mf) = \frac{S_{F_2\ddot{Z}_m}}{S_{F_2F_2}(mf)},$$

$$H_{17}(mf) = \frac{S_{F_3\ddot{Z}_m}}{S_{F_3F_3}(mf)}, \quad H_{18}(mf) = \frac{S_{F_4\ddot{Z}_m}}{S_{F_4F_4}(mf)}, \quad H_{21}(mf) = \frac{S_{\dot{Z}_{r_1}\ddot{\theta}_s}(mf)}{S_{\dot{Z}_{r_1}\dot{Z}_{r_1}}(mf)}, \tag{15}$$

$$H_{22}(mf) = \frac{S_{\dot{Z}_{r_2}\ddot{\theta}_s}(mf)}{S_{\dot{Z}_{r_2}\dot{Z}_{r_2}}(mf)}, \quad H_{23}(mf) = \frac{S_{\dot{Z}_{r_3}\ddot{\theta}_s}(mf)}{S_{\dot{Z}_{r_3}\dot{Z}_{r_3}}(mf)}, \quad H_{24}(mf) = \frac{S_{\dot{Z}_{r_4}\ddot{\theta}_s}(mf)}{S_{\dot{Z}_{r_4}\dot{Z}_{r_4}}(mf)},$$

$$H_{25}(mf) = \frac{S_{F_1\ddot{\theta}_s}(mf)}{S_{F_1F_1}(mf)}, \quad H_{26}(mf) = \frac{S_{F_2\ddot{\theta}_s}(mf)}{S_{F_2F_2}(mf)}, \quad H_{27}(mf) = \frac{S_{F_3\ddot{\theta}_s}(mf)}{S_{F_3F_3}(mf)},$$

$$H_{28}(mf) = \frac{S_{F_4\ddot{\theta}_s}(mf)}{S_{F_4F_4}(mf)}, \quad H_{31}(mf) = \frac{S_{\dot{Z}_{r_1}\ddot{\phi}_s}(mf)}{S_{\dot{Z}_{r_1}\dot{Z}_{r_1}}(mf)}, \quad H_{32}(mf) = \frac{S_{\dot{Z}_{r_2}\ddot{\phi}_s}(mf)}{S_{\dot{Z}_{r_2}\dot{Z}_{r_2}}(mf)},$$

$$H_{33}(mf) = \frac{S_{\dot{Z}_{r_3}\ddot{\phi}_s}(mf)}{S_{\dot{Z}_{r_3}\dot{Z}_{r_3}}(mf)}, \quad H_{34}(mf) = \frac{S_{\dot{Z}_{r_4}\ddot{\phi}_s}(mf)}{S_{\dot{Z}_{r_4}\dot{Z}_{r_4}}(mf)}, \quad H_{35}(mf) = \frac{S_{F_1\ddot{\phi}_s}(mf)}{S_{F_1F_1}(mf)},$$

$$H_{36}(mf) = \frac{S_{F_2\ddot{\phi}_s}(mf)}{S_{F_2F_2}(mf)}, \quad H_{37}(mf) = \frac{S_{F_3\ddot{\phi}_s}(mf)}{S_{F_3F_3}(mf)}, \quad H_{38}(mf) = \frac{S_{F_4\ddot{\phi}_s}(mf)}{S_{F_4F_4}(mf)}.$$

The estimated FRFs using (15) are shown in Figure 6. Such FRFs can be represented in a rational form by following [36] as,

$$H(z,\theta) = \frac{S_{\mathrm{m}}(z,\theta)}{U(z,\theta)} = \frac{\sum_{r=0}^{n_b} b_r z^{-r}}{\sum_{r=0}^{n_a} a_r z^{-r}}, \tag{16}$$

where a_r, b_r are the polynomial coefficients of poles and zeros respectively, and $\theta = [a_0\ a_1\ \cdots\ a_{n_a}\ b_0\ b_1\ \cdots\ b_{n_b}]^{\mathrm{T}}$. Now by using (8) and (16), we can write the input–output function as,

$$\begin{aligned} S_m^k(z) &= \sum_{i=0}^{N_p} \theta_i\, U_{k-i}(z), \\ Y_m^k(z) &= S_m^k(z) + \nu_k = \sum_{i=0}^{N_p} \theta_i\, U_{k-i}(z) + \nu_k, \\ Y_m^k(z) &= T_k(z)\, \theta_k(z) + \nu_k, \end{aligned} \tag{17}$$

where,

$$\underbrace{\begin{bmatrix} Y_m^N \\ Y_m^{(N-1)} \\ \vdots \\ Y_m^{(N_p)} \\ \vdots \\ Y_m^2 \\ Y_m^1 \end{bmatrix}}_{Y_m} = \underbrace{\begin{bmatrix} U^{(N-1)} & U^{(N-2)} & \cdots & U^{(N-N_p+1)} & U^{(N-N_p)} \\ U^{(N-2)} & U^{(N-3)} & \cdots & U^{(N-N_p)} & U^{(N-N_p-1)} \\ \vdots & \vdots & & \vdots & \\ U^{(N_p-1)} & U^{(N_p-2)} & \cdots & U^{1} & U^{0} \\ \vdots & \vdots & & \vdots & \\ U^{1} & U^{0} & \cdots & U^{(2-N_p+1)} & U^{(2-N_p)} \\ U^{0} & U^{-1} & \cdots & U^{(1-N_p+1)} & U^{(1-N_p)} \end{bmatrix}}_{T} \underbrace{\begin{bmatrix} b_1 \\ b_2 \\ \vdots \\ b_{N_p-1} \\ \vdots \\ b_{N_p} \end{bmatrix}}_{\theta} + \underbrace{\begin{bmatrix} \nu^N \\ \nu^{(N-1)} \\ \vdots \\ \nu^{(N_p)} \\ \vdots \\ \nu^2 \\ \nu^1 \end{bmatrix}}_{\nu}.$$

We are now able to rewrite the system as a series of output and input measurements Y_m^k and U_{k-i} at each sample $k = N$ with an undefined number of coefficients θ_i equal to N_p.

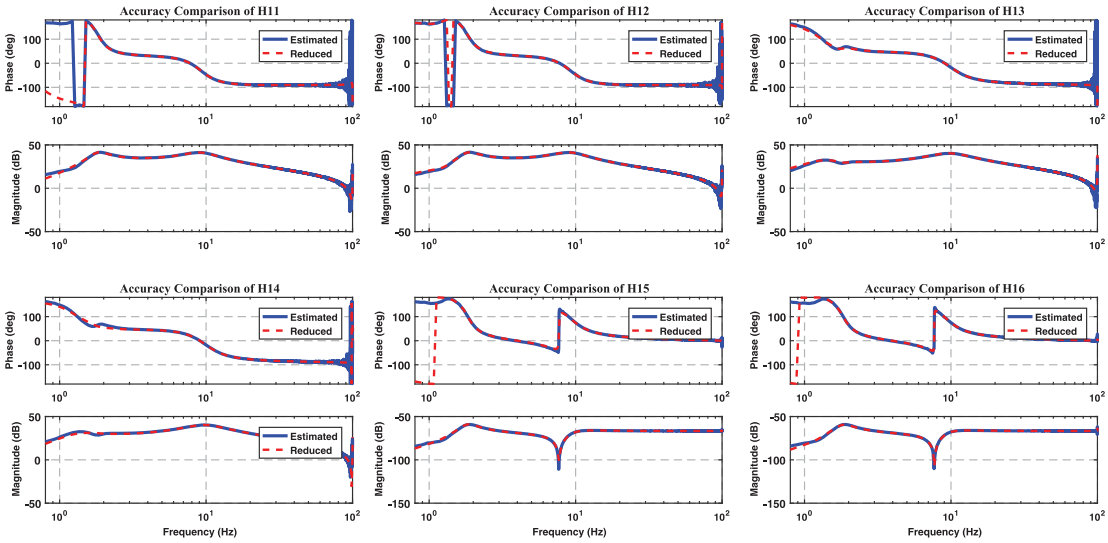

Figure 6. Comparison between some of the estimated and the reduced frequency response functions.

We are ready to solve these equations by applying the weighted least-squares approach to (17) for estimating coefficients $\hat{\theta}_{WLS}$, where the weighted matrix will be the series of coherence values γ^2_{yu} which measures how the response is correlated to the excitation,

$$\begin{aligned}
\text{Coherence} : \gamma^2_{\text{yu}}(mf) &= \frac{|S_{\text{yu}}(mf)|^2}{S_{\text{uu}}(mf)S_{\text{yy}}(mf)}, \\
\text{Estimated measurement} : \hat{Y}^k_m(z) &= T_k(z)\hat{\theta}_k(z), \\
\text{Estimated measurementerror} : \tilde{Y}^k_m(z) &= Y^k_m(z) - \hat{Y}^k_m(z),
\end{aligned} \tag{18}$$

In order to have a good model estimator, the estimated measurement error in (18) should be very small as an indication that the proposed estimated signals equal the true value. So, the cost function will be in the quadratic form as follows,

$$J_{WLS} := [\tilde{Y}^k_m]^{\text{T}} \, (\gamma^2_{\text{yu}})^k \, \tilde{Y}^k_m.$$

Taking now the gradient, $(\partial J_{WLS})/(\partial \hat{\theta}_{WLS}) = 0$ we get the following,

$$\hat{\theta}_{WLS} = \left[T_k^{\text{T}} \, (\gamma^2_{\text{yu}})^k \, T_k \right]^{-1} T_k^{\text{T}} \, (\gamma^2_{\text{yu}})^k \, T_k. \tag{19}$$

Remark 1: Note that the poles in the z-domain for all transfer functions are estimated by solving (19). Theoretically, all 24 transfer functions must have the exact same set of poles since they are all associated with the same dynamical system. But, each transfer function was estimated independently, the poles may not be exactly at the same locations as shown in Figure 7. For that reason, we will use a model reduction technique to eliminate the weak states which will have small effect on the overall response.

The derived reduced model is based on the Hankel singular values for the estimated model by using the Lyapunov balancing model [37]. The Hankel singular values σ_i can be

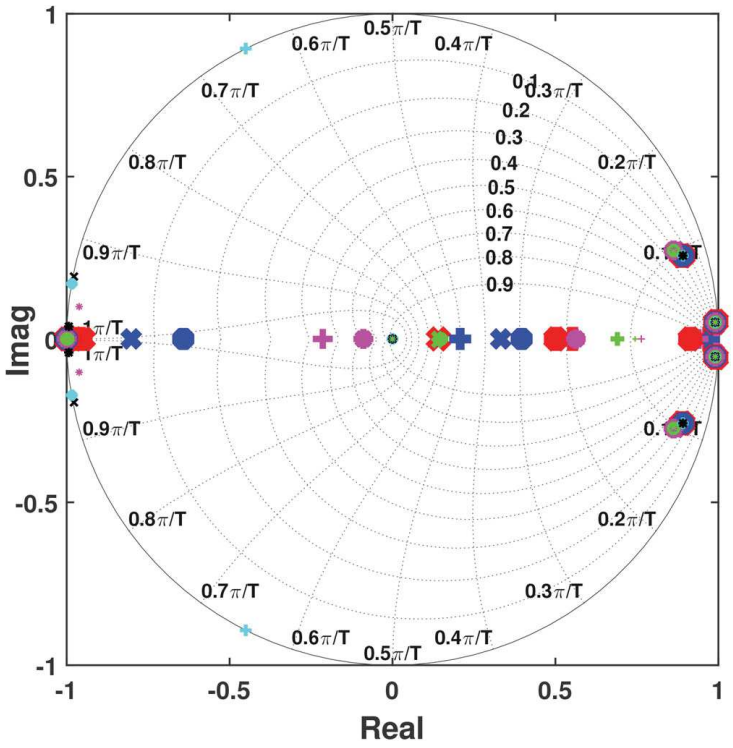

Figure 7. The locations of the poles of all the transfer functions in the Z-domain. It is shown that the poles for different transfer function are clustered at the same locations.

computed as,

$$\sigma_i = \sqrt{\lambda_i(\mathcal{P}\mathcal{O})},$$

$$\mathcal{P}(\hat{A}_d, \hat{B}_d) = \begin{bmatrix} \hat{B}_d & \hat{A}_d\hat{B}_d & \dots & \hat{A}_d^{n-1}\hat{B}_d \end{bmatrix}, \quad \mathcal{O}(\hat{A}_d, \hat{C}_d) = \begin{bmatrix} \hat{C}_d \\ \hat{C}_d\hat{A}_d \\ \vdots \\ \hat{C}_d^{n-1}\hat{A}_d \end{bmatrix},$$

where $\lambda_i(\cdot)$ is the eigenvalues of the product of controllability and observability Gramians $\mathcal{P}$, and $\mathcal{O}$ respectively. The relative strength for each state in the estimated model is shown in Figure 8. Based on the strongest 14 states, the reduced model is calculated and evaluated as shown in Figure 6, which demonstrates the accuracy of the reduced model in comparison with the estimated model.

4. Optimisation-based control

In this section, the duality between the Kalman filter and the linear quadratic regulator (LQR) is used as a tool for improving the ride comfort and the road holding stability of a full vehicle model.

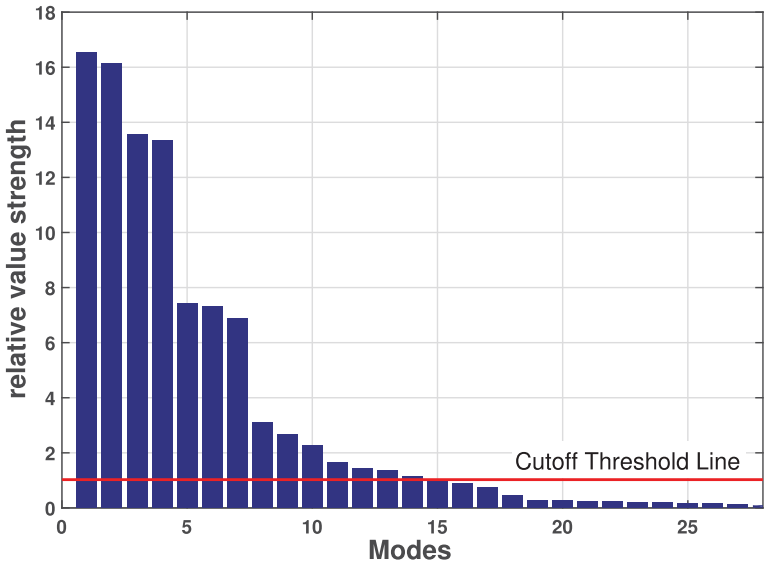

Figure 8. The Hankel singular values for each state. The model reduction has been calculated based on the 'strongest' 14 states while at the same time eliminating the 'weak' states which are under the cutoff threshold line.

4.1. Observer design

The goal of the observer is to estimate the plant states and dynamics with an acceptable level of accuracy at different driving and operating conditions. In order to achieve that, we will formulate an optimal output tracking problem.

Using (20) and (21), the observer dynamics are given by,

$$\hat{X}_{k+1} = \hat{A}_d \hat{X}_k + \hat{B}_{e_d} Q_k + \hat{B}_{f_d} F_k, \tag{20}$$

$$\hat{y}_k = \hat{C}_d \hat{X}_k + \hat{D}_{e_d} Q_k + \hat{D}_{e_d} F_k. \tag{21}$$

Remark 2: Note that the observer dynamics is the estimated model in Section 3, Where $\hat{A}_d$, $\hat{B}_{e_d}$, $\hat{B}_{f_d}$, $\hat{C}_d$, $\hat{D}_{e_d}$, $\hat{D}_{f_d}$ are the estimated discrete state matrices from the reduced model (see Figure 3). According to the well known separation principle the observer and the controller can be designed separately, i.e. the controller gain can be computed independently of the observer gain.

We assume that Q_k is the disturbance input for the actual plant and it is not available for measurement. We can then rewrite (20) and (21) as,

$$\hat{X}_{k+1} = \hat{A}_d \hat{X}_k + \hat{B}_{f_d} F_k + L(y_{m_k} - \hat{y}_k), \tag{22}$$

$$\hat{y}_k = \hat{C}_d \hat{X}_k + \hat{D}_{f_d} F_k, \tag{23}$$

where L is a correction term added to the observer states to achieve $y_{m_k} \to \hat{y}_k$.

It is desired to obtain the optimal value L which minimises the following cost function over infinite horizon,

$$J_L = \frac{1}{2}\sum_{k=0}^{\infty}[(y_{m_k} - \hat{y}_k)^{\mathrm{T}} M(y_{m_k} - \hat{y}_k) + L^{\mathrm{T}} RL], \tag{24}$$

where $R \succ 0, M \succeq 0$ are symmetric matrices. (24) can be solved in terms of the constraints (22) and (23) using optimal control theory [15,38].

The Hamiltonian for the system is,

$$H_L = \lambda^{\mathrm{T}}[\hat{A}_d\hat{X}_k + \hat{B}_{f_d}F_k + L(y_{m_k} - \hat{y}_k)] + \frac{1}{2}[(y_{m_k} - \hat{y}_k)^{\mathrm{T}} M(y_{m_k} - \hat{y}_k) + L^{\mathrm{T}} RL].$$

The optimal control can be found by using the stationarity condition $\frac{\partial H_L}{\partial L} = 0$ as follows,

$$L^* = -\left(R + \hat{B}_{f_d}^{\mathrm{T}} P\hat{B}_{f_d}\right)^{-1}$$
$$\hat{B}_{f_d}^{\mathrm{T}}\left(P\hat{A}_d\hat{X}_k + g\right).$$

Now, we need to solve the following coupled equations,

$$\hat{A}_d^{\mathrm{T}} P\hat{A}_d - P - \hat{A}_d^{\mathrm{T}} P\hat{B}_{f_d}\left(R^{-1} + \hat{B}_{f_d}^{\mathrm{T}} P\hat{B}_{f_d}\right)^{-1}\hat{B}_{f_d}^{\mathrm{T}} P\hat{A}_d + \hat{C}_d^{\mathrm{T}} M\hat{C}_d = 0, \tag{25}$$
$$g = \hat{A}_d^{\mathrm{T}}(I + P\hat{B}_{f_d}R^{-1}\hat{B}_{f_d}^{\mathrm{T}})^{-1}g - \hat{C}_d^{\mathrm{T}} My_{m_k}.$$

4.2. Control design

After estimating the plant states using the observer model, the controller can be computed by using LQR. In order to improve the ride comfort and the road holding stability, the aim of this controller is to minimise the sprung mass bounce, pitch and roll accelerations and the dynamic tire loads without violating the maximum limits of the rattle space by including the states in the weighted matrix M. In other words, the goal is to find a controller $F = [F_1, F_2, F_3, F_4]^{\mathrm{T}}$ that minimises the cost function ,

$$J_F = \frac{1}{2}\sum_{k=0}^{\infty}[\hat{X}_k^{\mathrm{T}} M\hat{X}_k + F_k^{\mathrm{T}} RF_k], \tag{26}$$

which can be solved in terms of the constraints (22) using the differential Riccati equation (25) to find G,

$$F_k = -G\hat{X}_k,$$

where,

$$G = \left(R^{-1} + \hat{B}_{f_d}^{\mathrm{T}} P\hat{B}_{f_d}\right)^{-1}\hat{B}_{f_d}^{\mathrm{T}} P\hat{A}_d,$$
$$\hat{A}_d^{\mathrm{T}} P\hat{A}_d - P - \hat{A}_d^{\mathrm{T}} P\hat{B}_{f_d}\left(R^{-1} + \hat{B}_{f_d}^{\mathrm{T}} P\hat{B}_{f_d}\right)^{-1}\hat{B}_{f_d}^{\mathrm{T}} P\hat{A}_d + M = 0.$$

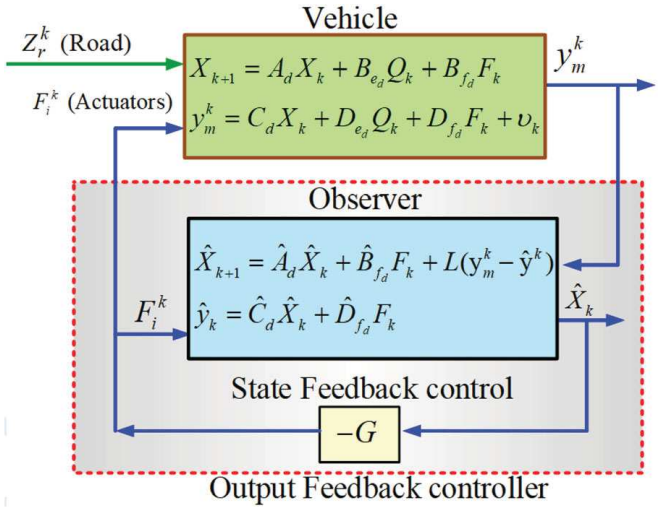

Figure 9. Optimal control diagram based on the augmented system of the actual vehicle model, the observer and the LQR state-feedback controller.

Based on the output-feedback controller design described in Figure 9, the augmented system has the following form,

$$\begin{bmatrix} X_{k+1} \\ \hat{X}_{k+1} \end{bmatrix} = \underbrace{\begin{bmatrix} A_d & -B_{f_d} G_k \\ L_k C_d & \hat{A}_d - L_k \hat{C}_d - \hat{B}_{f_d} G_k - L_k (D_{f_d} - \hat{D}_{f_d}) G_k \end{bmatrix}}_{A_{aug}} \begin{bmatrix} X_k \\ \hat{X}_k \end{bmatrix} + \underbrace{\begin{bmatrix} B_{e_d} \\ 0 \end{bmatrix}}_{B_{aug}} \begin{bmatrix} Z_{r_1}^k \\ Z_{r_2}^k \\ Z_{r_3}^k \\ Z_{r_4}^k \end{bmatrix} \tag{27}$$

$$\begin{bmatrix} y_{m_k} \\ \hat{y}_k \end{bmatrix} = \underbrace{\begin{bmatrix} C_d & -D_{f_d} G_k \\ 0 & \hat{C}_d - \hat{D}_{f_d} G_k \end{bmatrix}}_{C_{aug}} \begin{bmatrix} X_k \\ \hat{X}_k \end{bmatrix} + \underbrace{\begin{bmatrix} D_{e_d} \\ 0 \end{bmatrix}}_{D_{aug}} \begin{bmatrix} Z_{r_1}^k \\ Z_{r_2}^k \\ Z_{r_3}^k \\ Z_{r_4}^k \end{bmatrix} + \begin{bmatrix} \upsilon_k \\ 0 \end{bmatrix}. \tag{28}$$

5. Simulation results

In order to show the effectiveness and the robustness of the proposed framework, a numerical simulation has been used for validation. Where, we will firstly introduce two types of road excitation. Then, evaluating the observer performance for estimating the actual vehicle states with different CG uncertainties. Finally, demonstrating the LQG framework for controlling the active suspension system to improve the ride comfort and the road holding stability.

The vehicle parameters that were considered for the simulation are shown in Table 1. This vehicle is a passenger car adopted from [4] with maximum rattle space 8 cm. The Performance Index (PI) is assessed in terms of the following aspects:

Table 1. Vehicle parameters.

Sprung mass (m_s)	2160 kg
Front unsprung mass ($m_{1,2}$)	85 kg
Rear unsprung mass ($m_{3,4}$)	60 kg
Front spring stiffness (K_f)	96,861 N/m
Rear spring stiffness (K_r)	52,310 N/m
Tire spring stiffness (K_t)	200,000 N/m
Front damping coefficient (C_f)	2460 Ns/m
Rear damping coefficient (C_r)	2281 Ns/m
CG location from front axle (a)	1.524 (m)
CG location from rear axle (b)	1.156 (m)
Wheel track ($2w$)	1.450 (m)
Pitch mass moment of inertia (I_y)	4140 (kg m^2)
Roll mass moment of inertia (I_x)	946 (kg m^2)
Rattle space limit(Z_{max})	8 (cm)

- The peak and RMS values of the sprung mass accelerations;

$$RMS\left(\ddot{z}_{\mathrm{m}}, \ddot{\theta}_{\mathrm{s}}, \ddot{\phi}_{\mathrm{s}}\right) = \sqrt{\frac{1}{k}\sum_{i=1}^{k}\left(\ddot{z}_{\mathrm{m}}^{k}, \ddot{\theta}_{\mathrm{s}}^{k}, \ddot{\phi}_{\mathrm{s}}^{k}\right)^{2}}.$$

- The RMS values of the relative tire loads;

$$RMS\left(\eta_1, \eta_2, \eta_3, \eta_4\right) = \sqrt{\frac{1}{k}\sum_{i=1}^{k}\left(\eta_1^k, \eta_2,^k \eta_3^k, \eta_4^k\right)^{2}}.$$

- The peak values of the relative suspension deflection; $(\mu_1, \mu_2, \mu_3, \mu_4)$.

5.1. Road excitation

Two road profiles are considered for analysing the performance of the proposed scheme:

(1) A bumpy road profile.
(2) A road profile of class C of ISO-8608.

The two road profiles are applied to the actual system (4) and (8) with different vehicle speeds.

5.1.1. Bumpy road

This road profile consists of two successive sinusoidal road excitation signals as illustrated in (29) and in Figure 10(a). This formulation of road profile will introduce bounce, pitch and roll motion simultaneously and is given by,

$$\begin{aligned} z_{r_{1,2}} &= \begin{cases} \frac{h}{2}(1 - cos\ \omega t) & \text{if} \quad 0 \leqslant t \leqslant \frac{2\lambda}{V} \\ 0 \quad \text{otherwise,} \end{cases} \\ z_{r_{3,4}} &= \begin{cases} \frac{h}{2}(1 - cos\ \omega(t-\tau)) & \text{if } \tau \leqslant t \leqslant \left(\tau + \frac{2\lambda}{V}\right) \\ 0 \quad \text{otherwise,} \end{cases} \end{aligned} \tag{29}$$

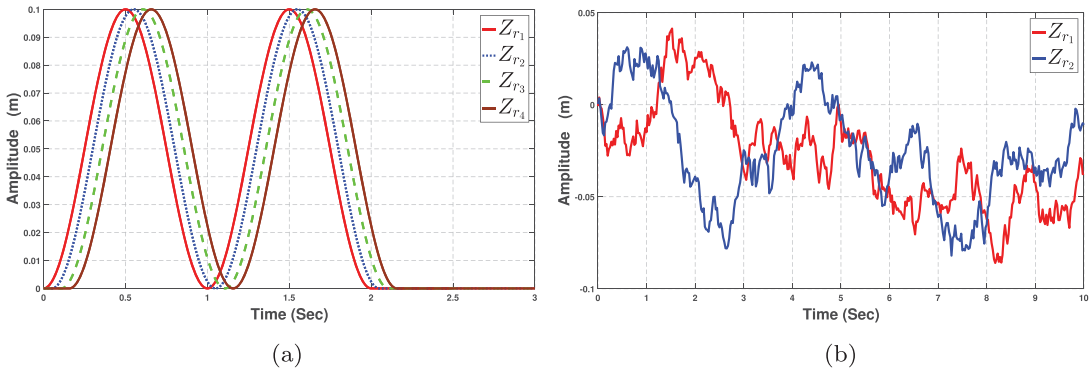

Figure 10. Two road profiles used for evaluating the proposed framework. (a) a bumpy road profile with vehicle speed 20 m/s, (b) ISO-8606 class C road profile with vehicle speed 10 m/s.

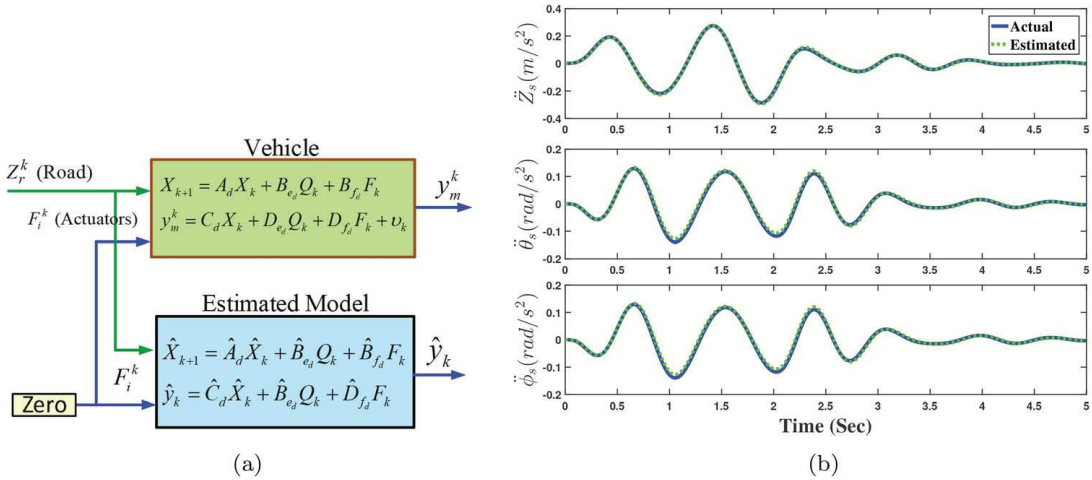

Figure 11. Open loop validation. It is shown that the response of the estimated model matches the response of the actual vehicle model. (a) The open loop diagram, (b) Comparison between actual and estimated model.

where, the bump height is $h = 0.1$ m with wave length $\lambda = 20$ m and the vehicle speed $V = 20$ m/s are used for the analysis, τ is the time lag between front and rear wheels, i.e. $\tau = (a + b)/V$, with ω is the road profile frequency, i.e. $\omega = (2\pi V)/\lambda$.This road profile has an amplitude of 10 cm, which is 25% higher than the rattle space limit.

5.1.2. ISO Class C road profile

According to ISO-8608, all roads are classified from class A to class H [39] based on the power spectral density (PSD) of the road profile. Class A road has a minor degree of roughness and class H are included all roads with a high degree of roughness.

The PSD of the road profile can be calculated as [40],

$$G_d(n) = G_d(n_0).\left(\frac{n}{n_0}\right)^{-2}, \tag{30}$$

where, $G_d(n_0)$ is the road roughness coefficient, n is the spatial frequency, n_0 is the reference spatial frequency. In this simulation, we selected class C road which can be classified as an average degree of road roughness as shown in Figure 10(b). Two different road profiles are

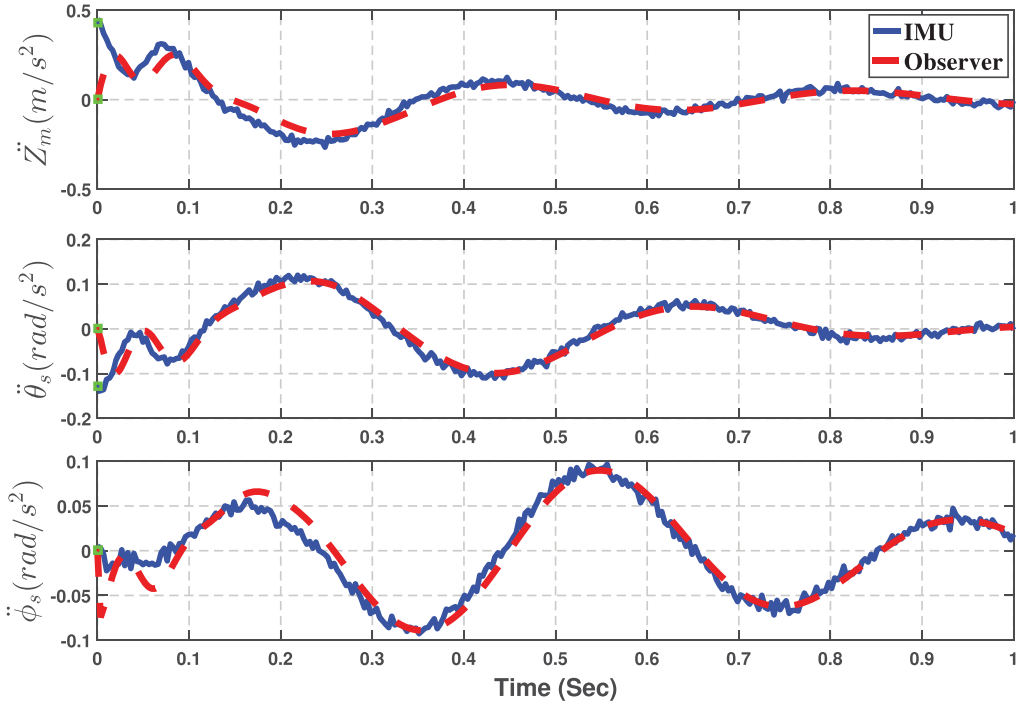

Figure 12. Observer behaviour.

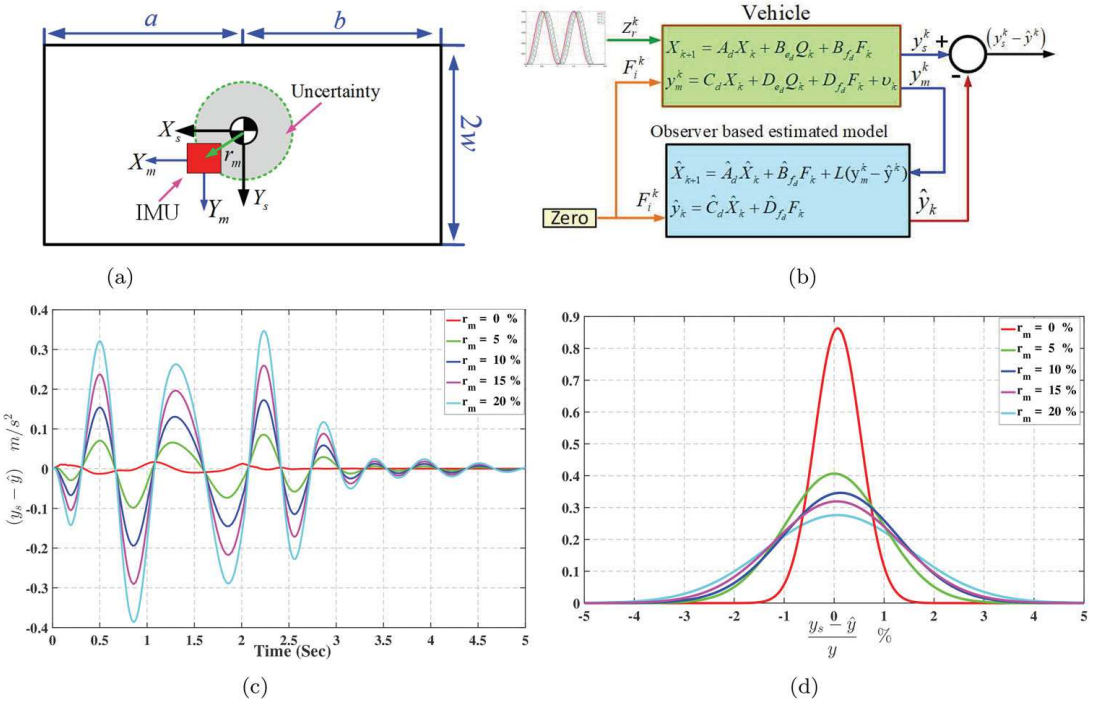

Figure 13. The robustness of the observer for estimating the actual states with 0%, 5%, 10%, 15% and 20% CG uncertainties. (a) CG position uncertainties, (b) Block digram for evaluating the model uncertainties, (c) Estimated error for different CG position uncertainties, (d) Probability distribution for the estimated error.

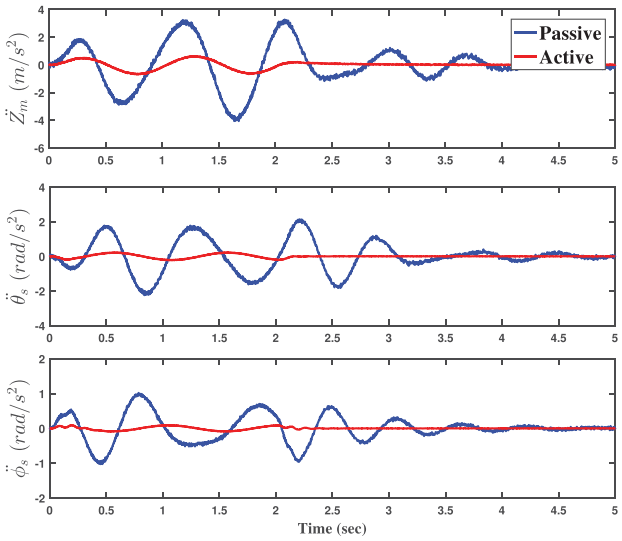

(a)

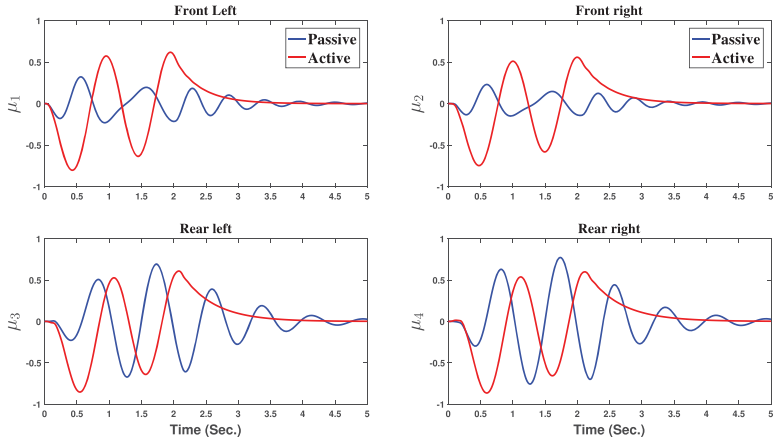

(b)

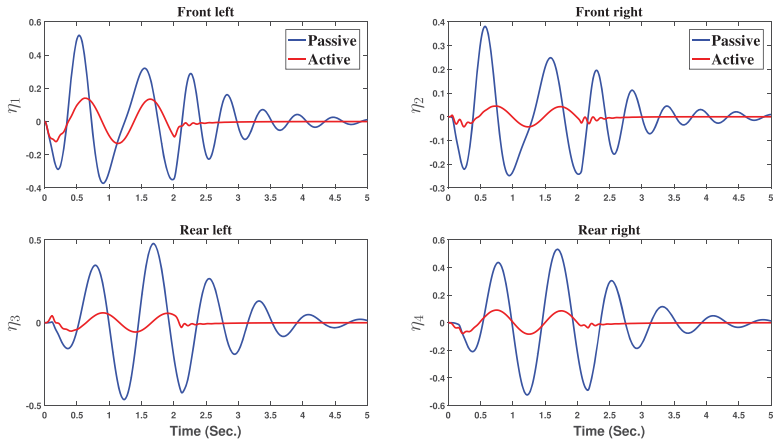

(c)

Figure 14. Comparison between active and passive system using a bumpy road profile. (a) sprung mass accelerations, (b) relative suspension deflection, (c) relative tire loads. It is shown that the sprung mass accelerations and the relative tire loads for the active suspension have been reduced within the limits of the available rattle space.

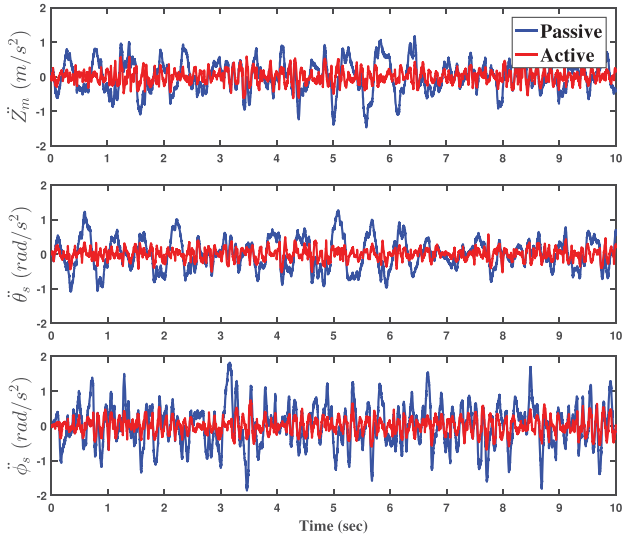

(a)

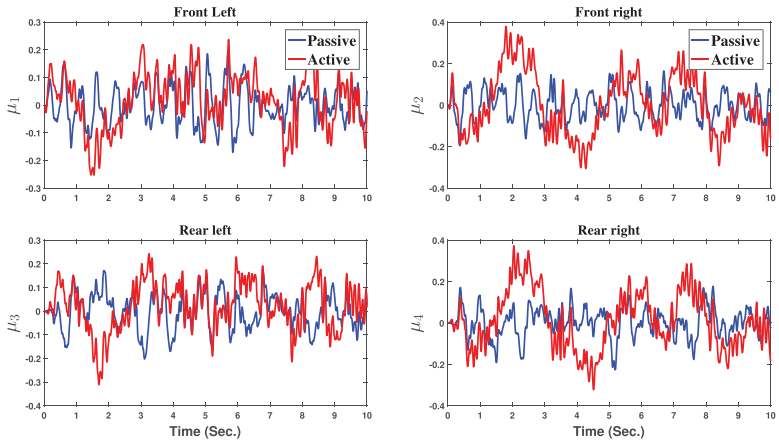

(b)

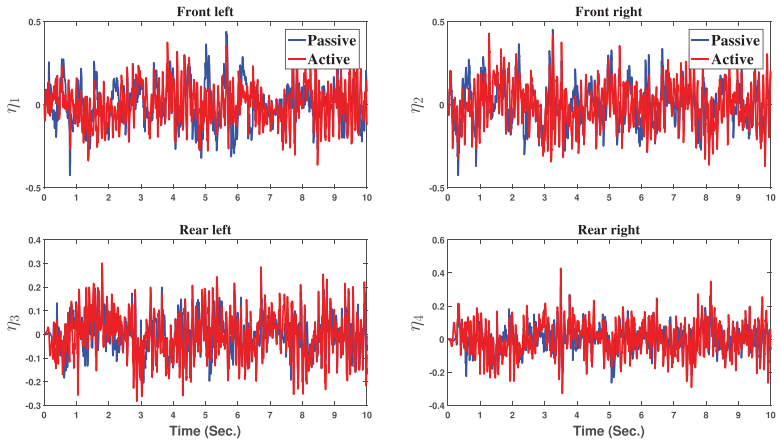

(c)

Figure 15. Comparison between active and passive system using ISO class C road profile. (a) sprung mass accelerations, (b) relative suspension deflection, (c) relative tire loads. It is shown that the sprung mass accelerations and the relative tire loads for the active suspension have been reduced within the limits of the available rattle space.

applied on front left tire and front right tire with a time lag τ between front and rear wheels, i.e. $\tau = (a + b)/V$, with vehicle speed $V = 10$ m/s.

5.2. Dynamic behaviour

In order to demonstrate the performance of the estimated model we applied the bumpy road profile as excitation signals to the actual and estimated models after setting the active suspension actuators to zero as shown in Figure 11(a).

The response of the actual and the estimated signals are demonstrated in Figure 11(b), where it reveals a successful matching between the estimated model and the actual model. The estimated model from Section 3 succeeded to capture the actual vehicle dynamics in estimating the sprung mass accelerations, which will allow using this estimated model in controlling the active suspension system of the actual vehicle to improve the ride comfort and road holding stability.

The observer behaviour using the Kalman filter is evaluated first by setting the actual model at different initial conditions with respect to the estimated model. It can be seen from Figure 12 that the observer succeeded to track the actual model after 0.3 second.

In order to evaluate the accuracy of the observer for robustly estimating the actual vehicle states with CG uncertainties, we calculated the estimated error, $y_s - \hat{y}$, for different positions of IMU as shown in Figure 13. We evaluated the observer behaviour with $r_m = 0\%, 5\%, 10\%, 15\%$ and 20% with respect to the CG position. The results of the estimated error and its probability distribution illustrate that the observer can estimate the actual behaviour of the vehicle model with 95% accuracy with up to 20% CG uncertainty.

In terms of evaluating the improvement of ride comfort and road holding stability of the active system over the passive system, we firstly applied the bumpy road profile to the proposed augmented system in (27) and (28). It can be seen from Figure 14 that the Kalman filter and LQR succeed to minimise the sprung mass accelerations and the relative tire loads within the limits of the suspension rattle space.

Figure 15 shows the results of sprung mass accelerations, relative suspension deflection and relative tire loads using ISO class C road profile. The proposed controller scheme gives a better ride comfort than the passive system and keeps the relative tire loads and the

Table 2. Summary of simulation results for the two road profiles.

		Bumpy road		ISO road	
Performance index	Measure	Passive	Active	Passive	Active
Ride comfort	Peak $\ddot{Z}_m$	3.855	0.662	1.397	0.624
	RMS $\ddot{Z}_m$	1.638	0.302	0.454	0.193
	Peak $\ddot{\theta}_s$	2.163	0.215	1.242	0.563
	RMS $\ddot{\theta}_s$	0.971	0.107	0.443	0.164
	Peak $\ddot{\phi}_s$	0.969	0.089	1.797	0.740
	RMS $\ddot{\phi}_s$	0.420	0.043	0.595	0.225
Road holding	RMS η_1	0.202	0.067	0.122	0.115
	RMS η_2	0.146	0.021	0.121	0.128
	RMS η_3	0.217	0.029	0.071	0.092
	RMS η_4	0.249	0.042	0.072	0.095
Rattle space	Peak μ_1	0.322	0.802	0.198	0.252
	Peak μ_2	0.230	0.747	0.192	0.379
	Peak μ_3	0.690	0.854	0.202	0.310
	Peak μ_4	0.772	0.865	0.226	0.372

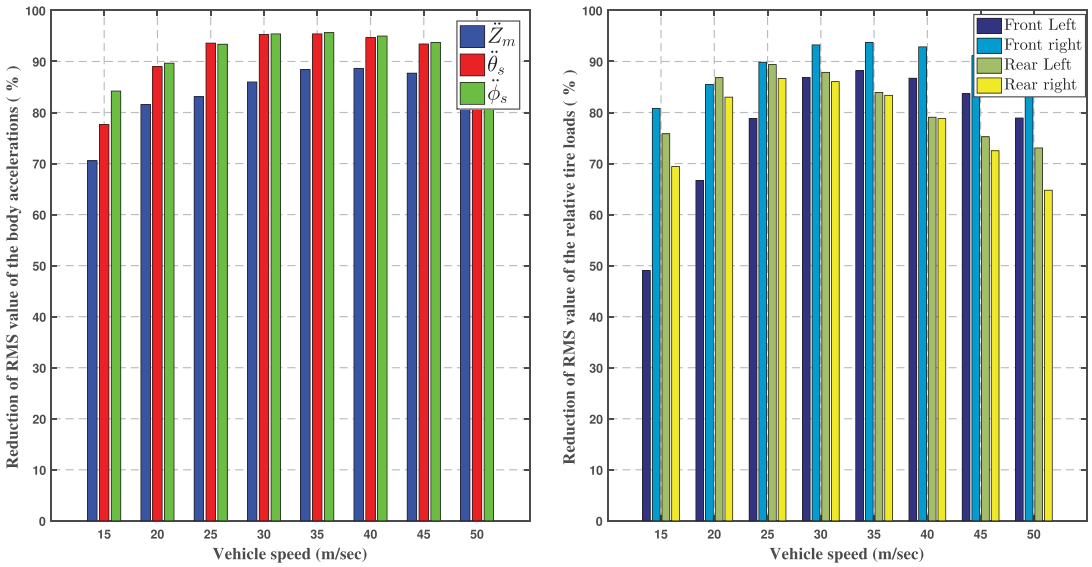

Figure 16. Improvement of ride comfort and road holding stability based on active suspension. It is shown that the sprung mass accelerations and the relative tire loads have been reduced at different vehicle speed with respect to passive system.

relative suspension deflections within the hard limits to ensure road holding stability and safety. the simulation results for the two road profiles are summarised in Table 2.

The robustness of the proposed approach was examined through a parametric study. The reduction of the RMS values of the sprung mass accelerations and the dynamic tire loads are evaluated with different vehicle speeds from 15 up to 50 m/s using the bumpy road profile. The results are illustrated in Figure 16, where the average reduction of RMS values for the sprung mass accelerations and the relative tire loads were not significantly impacted by the vehicle speed which ascertain the applicability of the proposed approach in estimating the vehicle dynamics with simultaneously improving the ride comfort and road holding stability.

6. Conclusion

The vehicle dynamics estimation and optimal control techniques are introduced for a full vehicle active suspension system using a noisy IMU with CG position uncertainties. We have estimated the dynamics and the states by using system identification techniques on separate channels. Such identification techniques used excitation signals that let us to estimate the system transfer functions. The response of the estimated model shows satisfactory performance in the presence of measurement uncertainties with a 95% accuracy. Then, an output-feedback controller was designed to improve ride comfort and road holding stability. Finally, simulation results are presented to demonstrate the efficiency and quantified performance of the proposed scheme. Future work will focus on applying plug-n-play learning techniques that do not require any offline computations to the actual nonlinear model.

Disclosure statement

No potential conflict of interest was reported by the authors.

Funding

This material is based upon work supported in part by North Atlantic Treaty Organization (NATO) [grant number SPS G5176] and by NSF CAREER [grant number CPS-1750789].

ORCID

Tamer Attia https://orcid.org/0000-0002-3393-6687
Kyriakos G. Vamvoudakis https://orcid.org/0000-0003-1978-4848
Tomonari Furukawa http://orcid.org/0000-0003-2811-4221

References

[1] Čorić M, Deur J, Xu L, et al. Optimisation of active suspension control inputs for improved vehicle ride performance. Vehicle Syst Dyn. 2016;54(7):1004–1030.
[2] Sun W, Gao H, Yao B. Adaptive robust vibration control of full-car active suspensions with electrohydraulic actuators. IEEE Trans Control Syst Technol. 2013;21(6):2417–2422.
[3] Katsuyama E, Omae A. Improvement of ride comfort by unsprung negative skyhook damper control using in-wheel motors. SAE Int J Altern Powertrains. 2016;5(2016-01-1678):214–221.
[4] Shirahatti A, Prasad P, Panzade P, et al. Optimal design of passenger car suspension for ride and road holding. J Braz Soc Mech Sci Eng. 2008;30(1):66–76.
[5] Lu J, DePoyster M. Multiobjective optimal suspension control to achieve integrated ride and handling performance. IEEE Trans Control Syst Technol. 2002;10(6):807–821.
[6] Ajaj M, Sharaf A, Hegazy S, et al. Investigation of control algorithms for semi-active suspension systems based on a full vehicle model. ASME 2011 International Mechanical Engineering Congress and Exposition. American Society of Mechanical Engineers; 2011. p. 187–197.
[7] Deshpande VS, Shendge P, Phadke S. Dual objective active suspension system based on a novel nonlinear disturbance compensator. Vehicle Syst Dyn. 2016;54(9):1269–1290.
[8] Wong JY. Theory of ground vehicles. Hoboken (NJ): John Wiley & Sons; 2008.
[9] Chen W, Xiao H, Wang Q, et al. Integrated vehicle dynamics and control. Singapore: John Wiley & Sons; 2016.
[10] Bouazara M, Richard MJ. An optimization method designed to improve 3-d vehicle comfort and road holding capability through the use of active and semi-active suspensions. Eur J Mech-A/Solids. 2001;20(3):509–520.
[11] Huang Y, Na J, Wu X, et al. Adaptive control of nonlinear uncertain active suspension systems with prescribed performance. ISA Trans. 2015;54:145–155.
[12] Tseng HE, Hrovat D. State of the art survey: active and semi-active suspension control. Vehicle Syst Dyn. 2015;53(7):1034–1062.
[13] Yamada F, Suzuki K, Toda T, et al. Robust control of active suspension to improve ride comfort with structural constraints. 2016 IEEE 14th International Workshop on Advanced Motion Control (AMC). IEEE; 2016. p. 103–108.
[14] Spirk S, Lohmann B. Controlling an active suspension using methods of optimal control. 2012 IEEE 51st Annual Conference on Decision and Control (CDC). IEEE; 2012. p. 6333–6339.
[15] Lewis FL, Vrabie D, Syrmos VL. Optimal control. New York (NY): John Wiley & Sons; 2012.
[16] Thenmozhi S, Rajeswari K. Kalman estimator for an active suspension system. 2012 International Conference on Advances in Engineering, Science and Management (ICAESM). IEEE; 2012. p. 155–160.
[17] Na J, Herrmann G, Vamvoudakis KG. Adaptive optimal observer design via approximate dynamic programming. American Control Conference (ACC); 2017. IEEE; 2017. p. 3288–3293.
[18] Attia T, Kochersberger K, Bird J, Southward SC. System identification and optimal control of half-car active suspension system using a single noisy imu with position uncertainty. ASME 2017 Dynamic Systems and Control Conference. American Society of Mechanical Engineers; 2017. p. V002T04A002–V002T04A002.

[19] Wenzel TA, Burnham K, Blundell M, et al. Dual extended kalman filter for vehicle state and parameter estimation. Vehicle Sys Dyn. 2006;44(2):153–171.
[20] Koch G, Kloiber T, Lohmann B. Nonlinear and filter based estimation for vehicle suspension control. 2010 IEEE 49th Conference on Decision and Control (CDC). IEEE; 2010. p. 5592–5597.
[21] Pletschen N, Diepold KJ. Nonlinear state estimation for suspension control applications: a takagi-sugeno kalman filtering approach. Control Eng Pract. 2017;61:292–306.
[22] Pletschen N, Barthelmes S, Lohmann B. Joint state-parameter estimation for active vehicle suspensions: a takagi-sugeno kalman filtering approach. 2015 IEEE 54th Annual Conference on Decision and Control (CDC). IEEE; 2015. p. 1545–1550.
[23] Pletschen N, Badur P. Nonlinear state estimation in suspension control based on takagi-sugeno model. IFAC Proc Vol. 2014;47(3):11231–11237.
[24] Graf C, Kieneke R, Maas J. Online force estimation for an active suspension control. 2012 IEEE/ASME International Conference on Advanced Intelligent Mechatronics (AIM). IEEE; 2012. p. 544–549.
[25] García SD, Patino D. Estimation based on acceleration measures of an active suspension plant. 2015 IEEE 2nd Colombian Conference on Automatic Control (CCAC). IEEE; 2015. p. 1–6.
[26] Thaller S, Reiterer F, Schmied R, et al. Fast determination of vehicle suspension parameters via continuous time system identification. IFAC-PapersOnLine. 2016;49(11):448–453.
[27] Mastinu G, Plöchl M. Road and off-road vehicle system dynamics handbook. Boca Raton: CRC Press; 2014.
[28] Healey A, Nathman E, Smith C. An analytical and experimental study of automobile dynamics with random roadway inputs. J Dyn Syst Meas Control. 1977;99(4):284–292.
[29] Smith R, Sigman D. Experimental verification of a linear rigid body model. Ford Motor Company Research Report. Dearborn, MI, October 1981.
[30] Jazar RN. Vehicle dynamics: theory and applications. New York (NY): Springer-Verlag; 2008.
[31] Liu H, Gao H, Li P. Handbook of vehicle suspension control systems. Inst Eng Technol. 2013.
[32] Rajamani R. Vehicle dynamics and control. New York (NY): Springer Science & Business Media; 2011.
[33] Oppenheim AV. Discrete-time signal processing third edition. Upper Saddle River (NJ): Pearson Higher Education; 2010.
[34] Ljung L. System identification. In: Signal analysis and prediction. Springer; 1998. p. 163–173.
[35] Frigo M, Johnson SG. Fftw: an adaptive software architecture for the fft. 1998. Proceedings of the 1998 IEEE International Conference on Acoustics, Speech and Signal Processing. Vol. 3. IEEE; 1998. p. 1381–1384.
[36] Pintelon R, Schoukens J. System identification: a frequency domain approach. Hoboken (NJ): John Wiley & Sons; 2012.
[37] Gugercin S, Antoulas AC. A survey of balancing methods for model reduction. European Control Conference (ECC). IEEE; 2003. p. 968–973.
[38] Lin F. Robust control design: an optimal control approach. 18. Chichester: John Wiley & Sons; 2007.
[39] ISO-8608. Mechanical vibration – road surface profiles – reporting of measured data. 1995.
[40] Agostinacchio M, Ciampa D, Olita S. The vibrations induced by surface irregularities in road pavements–a matlab approach. Eur Transp Res Rev. 2014;6(3):267–275.

Appendix. State-space representation of vehicle model

The matrices $A, B_e, B_f, C, D_e, D_f, Q, F$ are defined according to the sate-space representation of vehicle model in Section 2 as follows,

$$A = \begin{bmatrix} A_1 & A_2 & \cdots & A_{14} & A_{15} \end{bmatrix}.$$

Where,

$$A_1 = \begin{bmatrix} 0&0&0&0&0&0&0&0&1&-a&w&-1&0&0&0 \end{bmatrix}, \quad A_2 = \begin{bmatrix} 0&0&0&0&0&0&0&0&1&-a&-w&0&-1&0&0 \end{bmatrix},$$

$$A_3 = \begin{bmatrix} 0&0&0&0&0&0&0&0&1&b&w&0&0&-1&0 \end{bmatrix}, \quad A_4 = \begin{bmatrix} 0&0&0&0&0&0&0&0&1&b&-w&0&0&0&-1 \end{bmatrix},$$

$$A_5 = \begin{bmatrix} 0&0&0&0&0&0&0&0&0&0&0&0&1&0&0&0 \end{bmatrix}, \quad A_6 = \begin{bmatrix} 0&0&0&0&0&0&0&0&0&0&0&0&0&1&0&0 \end{bmatrix},$$

$$A_7 = \begin{bmatrix} 0&0&0&0&0&0&0&0&0&0&0&0&0&0&1&0 \end{bmatrix}, \quad A_8 = \begin{bmatrix} 0&0&0&0&0&0&0&0&0&0&0&0&0&0&0&1 \end{bmatrix},$$

$$A_9 = \frac{1}{m_s}\begin{bmatrix} -k_f \\ -k_f \\ -k_r \\ -k_r \\ 0 \\ 0 \\ 0 \\ 0 \\ -2(c_f + c_r) \\ 2(ac_f - bc_r) \\ 0 \\ c_f \\ c_f \\ c_r \\ c_r \end{bmatrix}^{\mathrm{T}}, \quad A_{10} = \frac{1}{I_y}\begin{bmatrix} ak_f \\ ak_f \\ bk_r \\ bk_r \\ 0 \\ 0 \\ 0 \\ 0 \\ 2(ac_f - bc_r) \\ -2(a^2c_f + b^2c_r) \\ 0 \\ -ac_f \\ -ac_f \\ bc_r \\ bc_r \end{bmatrix}^{\mathrm{T}}, \quad A_{11} = \frac{w}{I_x}\begin{bmatrix} -k_f \\ k_f \\ -k_r \\ k_r \\ 0 \\ 0 \\ 0 \\ 0 \\ 0 \\ 0 \\ -2w(c_f + c_r) \\ c_f \\ -c_f \\ c_r \\ -c_r \end{bmatrix}^{\mathrm{T}},$$

$$A_{12} = \frac{1}{m_f}\begin{bmatrix} k_f \\ 0 \\ 0 \\ 0 \\ -k_t \\ 0 \\ 0 \\ 0 \\ c_f \\ -ac_f \\ wc_f \\ -c_f \\ 0 \\ 0 \\ 0 \end{bmatrix}^{\mathrm{T}}, \quad A_{13} = \frac{1}{m_f}\begin{bmatrix} 0 \\ k_f \\ 0 \\ 0 \\ 0 \\ -k_t \\ 0 \\ 0 \\ c_f \\ -ac_f \\ -wc_f \\ 0 \\ -c_f \\ 0 \\ 0 \end{bmatrix}^{\mathrm{T}}, \quad A_{14} = \frac{1}{m_r}\begin{bmatrix} 0 \\ 0 \\ k_r \\ 0 \\ 0 \\ 0 \\ -k_t \\ 0 \\ c_r \\ bc_r \\ wc_r \\ 0 \\ 0 \\ -c_r \\ 0 \end{bmatrix}^{\mathrm{T}}, \quad A_{15} = \frac{1}{m_r}\begin{bmatrix} 0 \\ 0 \\ k_r \\ 0 \\ 0 \\ 0 \\ -k_t \\ 0 \\ 0 \\ 0 \\ c_r \\ bc_r \\ -wc_r \\ -c_r \end{bmatrix}^{\mathrm{T}},$$

$$B_e = \begin{bmatrix} 0 & 0 & 0 & 0 \\ 0 & 0 & 0 & 0 \\ 0 & 0 & 0 & 0 \\ 0 & 0 & 0 & 0 \\ -1 & 0 & 0 & 0 \\ 0 & -1 & 0 & 0 \\ 0 & 0 & -1 & 0 \\ 0 & 0 & 0 & -1 \\ 0 & 0 & 0 & 0 \\ 0 & 0 & 0 & 0 \\ 0 & 0 & 0 & 0 \\ 0 & 0 & 0 & 0 \\ 0 & 0 & 0 & 0 \\ 0 & 0 & 0 & 0 \\ 0 & 0 & 0 & 0 \end{bmatrix}, \quad B_f = \begin{bmatrix} 0 & 0 & 0 & 0 \\ 0 & 0 & 0 & 0 \\ 0 & 0 & 0 & 0 \\ 0 & 0 & 0 & 0 \\ 0 & 0 & 0 & 0 \\ 0 & 0 & 0 & 0 \\ 0 & 0 & 0 & 0 \\ 0 & 0 & 0 & 0 \\ \frac{1}{m_s} & \frac{1}{m_s} & \frac{1}{m_s} & \frac{1}{m_s} \\ \frac{-a}{I_y} & \frac{-a}{I_y} & \frac{b}{I_y} & \frac{b}{I_y} \\ \frac{w}{I_x} & \frac{-w}{I_x} & \frac{w}{I_x} & \frac{-w}{I_x} \\ \frac{-1}{m_f} & 0 & 0 & 0 \\ 0 & \frac{-1}{m_f} & 0 & 0 \\ 0 & 0 & \frac{-1}{m_r} & 0 \\ 0 & 0 & 0 & \frac{-1}{m_r} \end{bmatrix}.$$

And,

$$C = \begin{bmatrix} A_9 & A_{10} & A_{11} \end{bmatrix}^{\mathrm{T}}, \quad D_e = \begin{bmatrix} 0 & 0 & 0 & 0 \\ 0 & 0 & 0 & 0 \\ 0 & 0 & 0 & 0 \end{bmatrix}, \quad D_f = \begin{bmatrix} \frac{1}{m_s} & \frac{1}{m_s} & \frac{1}{m_s} & \frac{1}{m_s} \\ \frac{-a}{I_y} & \frac{-a}{I_y} & \frac{b}{I_y} & \frac{b}{I_y} \\ \frac{w}{I_x} & \frac{-w}{I_x} & \frac{w}{I_x} & \frac{-w}{I_x} \end{bmatrix}.$$